



HAL
open science

Investigation of subgrains in directionally solidified cast mono-seeded silicon and their interactions with twin boundaries

Maike Becker, Etienne Pihan, Fabrice Guittonneau, Laurent Barrallier, Gabrielle Regula, Hadjer Ouaddah, Guillaume Reinhart, Nathalie Mangelinck-Noël

► To cite this version:

Maike Becker, Etienne Pihan, Fabrice Guittonneau, Laurent Barrallier, Gabrielle Regula, et al.. Investigation of subgrains in directionally solidified cast mono-seeded silicon and their interactions with twin boundaries. *Solar Energy Materials and Solar Cells*, 2020, 218, pp.110817. hal-03169396

HAL Id: hal-03169396

<https://hal.science/hal-03169396v1>

Submitted on 15 Mar 2021

HAL is a multi-disciplinary open access archive for the deposit and dissemination of scientific research documents, whether they are published or not. The documents may come from teaching and research institutions in France or abroad, or from public or private research centers.

L'archive ouverte pluridisciplinaire **HAL**, est destinée au dépôt et à la diffusion de documents scientifiques de niveau recherche, publiés ou non, émanant des établissements d'enseignement et de recherche français ou étrangers, des laboratoires publics ou privés.

Investigation of subgrains in directionally solidified cast mono-seeded silicon and their interactions with twin boundaries

Maike Becker^{a*}, Etienne Pihan^b, Fabrice Guittonneau^c, Laurent Barrallier^c, Gabrielle Regula^a, Hadjer Ouaddah^a, Guillaume Reinhart^a, Nathalie Mangelinck-Noël^a

^a Aix Marseille Univ, Université de Toulon, CNRS, IM2NP, 13397, Marseille, France

^b Univ. Grenoble Alpes, INES, CEA, LITEN, Department of Solar Technologies, F-73375 Le Bourget du Lac, France

^c Arts et Métiers Paristech/Institut Carnot Arts Centre Aix-en-Provence 2, Cours des Arts et Métiers, 13617, Aix-en-Provence, Cedex 1, France

**email*: maike.becker@dlr.de

¹ Present address: Institut für Materialphysik im Weltraum, Deutsches Zentrum für Luft- und Raumfahrt, 51170 Köln, Germany

Keywords: silicon; cast mono; subgrain boundaries; dislocations; X-ray diffraction imaging; electron backscatter diffraction

Abstract

Directional solidification of a cast mono-seed and of a FZ-seed was performed and the grain and defect structures of the seeds as well as of the regrown parts are analyzed. *In situ* X-ray diffraction imaging enabled the observation of the dislocation arrangements. During the heating process, in the FZ-seed, mobile dislocations glide on $\{111\}$ planes, whereas in the cast mono seed dislocations are arranged in a mainly immobile cellular structure. *Ex situ* grain orientation mappings reveal the presence of subgrains with misorientations up to 3° in the regrown part of the cast mono-seeded sample, which are not observed in the regrown part of the FZ-seeded sample. Subgrain boundaries characterized by misorientations around the $[001]$ growth axis propagate roughly along the growth axis and increase their misorientation by merging with new subgrain boundaries appearing in their vicinity. Although the first inception of subgrain formation cannot be revealed, the comparison of the dislocation arrangements in the two seeds strongly suggests an influence of the latter on subgrain formation. In the regrown part, interactions between subgrain boundaries and twin boundaries show that they can follow $\Sigma 3\{111\}$ and $\Sigma 9\{221\}$ grain boundaries or cross $\Sigma 3\{111\}$ grain boundaries. Whether $\Sigma 3\{111\}$ GBs are crossed or not depends among other things on the orientation of the grains on either side of the twin. It demonstrates that the grain orientation relationship and not only the grain boundary character play an important role in the subgrain structure evolution and redistribution in a multicrystalline silicon ingot.

1. Introduction

Subgrain boundaries (SGBs) are known to be electrically active defects that decrease the photovoltaic (PV) efficiency and, therefore, should be limited during the manufacturing process [1]. SGBs consist of linear dislocation arrangements, as this configuration reduces the elastic energy in the crystal. In (100) grown crystals, SGBs can form during the directional solidification process by growing with the solid-liquid interface inducing a tilted subgrain structure with rotations parallel to the growth direction. The angular deviation of crystal orientations often increases with ingot height, as more dislocations of the

46 same character are incorporated in the SGBs [2, 3]. The orientation of the glide planes with respect to the
47 growth direction, their activation due to equivalent resolved shear stresses during solidification, but also
48 the generation and termination mechanisms determine the final dislocation distribution.

49 Subgrains are observed in all silicon ingots that are produced by casting processes for PV
50 applications: in cast mono (cm-Si) [4-6], high-performance multicrystalline (HPmc-Si), [7] and
51 conventional multicrystalline (mc-Si) silicon [8]. For mc-Si, either grains with $\langle 110 \rangle$ or $\langle 111 \rangle$ growth
52 directions were reported to have the highest dislocation density [8-10]. In cast mono-Si, however, the
53 $\langle 110 \rangle$ growth direction produced fewer dislocation clusters, i.e. narrower clusters originating at the seed
54 junctions than the $\langle 100 \rangle$ growth direction [11].

55 The origin of dislocation clusters is found to be at grain boundaries [12, 13], with $\Sigma 27a$ GBs [7, 9, 14]
56 and SGBs [15] playing a dominant role. Besides, dislocations in cast mono-Si are mainly generated at the
57 junctions of the seed pavement [16, 17]. Additionally, subgrains originate from dislocation alignments
58 already present in the seed crystals that can propagate into the new grown crystal during growth [18-20].
59 For the latter mechanism, the initial dislocation arrangement in cells in the seed is a main factor [19, 21]
60 and depends on the stress in the seed [22-24].

61 Additionally, it was found that the dislocation density in the newly grown crystal is at first lower than
62 in the un-melted seeds [17, 22]. On the one hand, it could indicate that the thermomechanical stresses
63 imposed on the seeds during the heating process are higher than during crystallization. On the other hand,
64 it must be considered that dislocation generation mechanisms in a seed and the newly grown crystal are
65 different and that dislocation mobility is strongly dependent on temperature and impurities. Therefore, it
66 is particularly important to control the crystal quality of the seeds in order to control the dislocations in
67 the regrown part.

68 Just as important to understand the formation of subgrains is to find out the reason for their
69 disappearance. A high amount of random angle GBs, like it exists in HPmc-Si, causes a decrease of the
70 amount of subgrains in the ingot, because it is inferred that the dislocations are stopped at these
71 boundaries [7]. It was also reported that neighbor grains with lower dislocation densities overgrow the
72 grains with higher cluster densities [8]. These observations show that once formed, the subgrains can only
73 be stopped by grain competition mechanisms, wherefore subgrain formation is highly undesirable in cast
74 mono growth for which this mechanism is irrelevant due to the absence of grain boundaries.

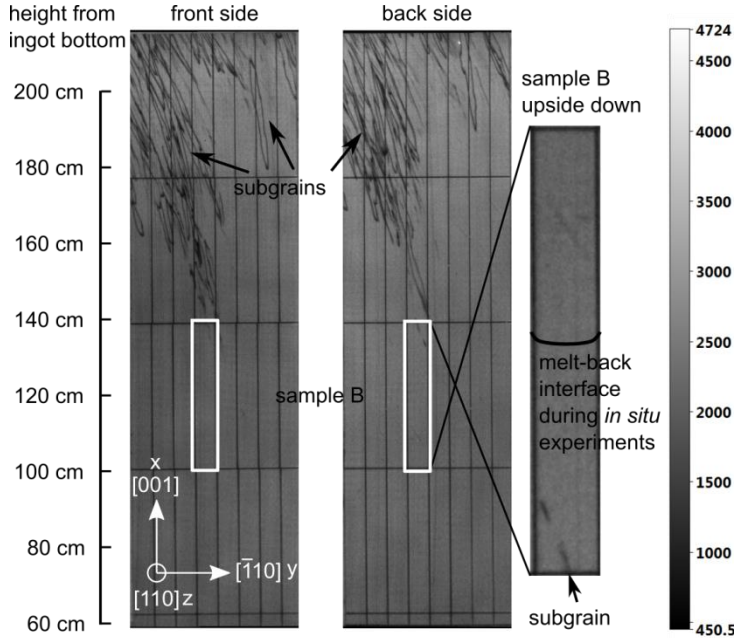
75 In order to better understand the role of the seed in the formation of subgrains, small-scale directional
76 solidification experiments using a float-zone (FZ) seed and a cast mono seed in [001] growth orientation
77 were performed. We compare the developed grain structure by applying *in situ* X-ray diffraction imaging
78 to monitor the solidification microstructure during growth and *ex situ* etch pit and electron backscatter
79 diffraction (EBSD) analysis to reveal the grain structure and defect spatial distribution. Formation of
80 SGBs in the cast mono-seeded sample is observed and discussed in terms of their formation, propagation
81 and disappearance.

82 2. Experimental methods

83 2.1. Sample preparation and processing

84 Two samples originating from different processing techniques are used as seeds for directional
85 solidification. Sample A-seed was produced by zone-melting using 9N material (SIL'TRONIX Silicon
86 Technologies). Accordingly, the impurity concentrations of oxygen and carbon are below 10^{15} at cm^{-3} .
87 The sample was cut with a diamond wire saw to a size of 38×7 mm and polished to a thickness of
88 0.3 mm. SiC abrasive paper followed by a $6 \mu\text{m}$ and a $3 \mu\text{m}$ diamond suspension was used for final
89 polishing.

90 Sample B-seed was produced by the cast mono directional solidification technique from Cz seeds.
 91 The casted ingot had a laboratory scale 85 kg G2 and was provided by the Institut National de l'Energie
 92 Solaire (INES). A photoluminescence (PL) image of a vertical wafer cut from which sample B was taken
 93 is shown in Fig. 1. A white border marks the sample position (100 cm - 140 cm from the bottom). It is
 94 taken just below the area where electrically active subgrains do appear on the PL maps. In order to study
 95 subgrain influence during growth, the sample was put upside down in the furnace before partial melting.
 96 The final melt-back interface during the experiments was still above the visible subgrains and is shown in
 97 black on the magnified sample B image. The impurity content in interstitial oxygen $[O_i]$ and substitutional
 98 carbon $[C_s]$ at the height of the sample is $(6 \pm 1) \times 10^{16} \text{ cm}^{-3}$ and $(4.5 \pm 0.6) \times 10^{17} \text{ cm}^{-3}$, respectively.
 99



100
 101 **Fig. 1** Photoluminescence (PL) image of a vertical cut of the source ingot of sample B. In the upper part, electrically
 102 active SGBs are visible as dark lines. Sample B was taken just below this area.

103 Both samples A and B have the same crystallographic orientation. The two main surfaces are the
 104 (110) and $(\bar{1}\bar{1}0)$ planes, the vertical side planes are $(1\bar{1}0)$ and $(\bar{1}10)$ and the horizontal planes are (001)
 105 and $(00\bar{1})$.

106 The samples were placed in a boron nitride crucible and processed in a high temperature Bridgman
 107 furnace known as GaTSBI (Growth at high Temperature observed by Synchrotron Beam Imaging) [e.g.
 108 25, 26]. First, the temperature of both heating elements was slowly increased from room temperature up
 109 to a temperature of 1100 °C. Then, a temperature gradient of 30 °C cm⁻¹ was applied to the heaters with
 110 $T_{\text{Top}} > T_{\text{Bottom}}$ and heating continued up to the melting point of silicon which is 1414 °C. The local vertical
 111 temperature gradient G_{local} in the sample was always lower than the applied temperature gradient G_{appl} and
 112 can be calculated with $G_{\text{local}} = T/\nu$ using the applied cooling rate \dot{T} and measuring the growth velocity of
 113 the solid-liquid interface ν [27, 28]. G_{local} was approximately $(14 \pm 3) \text{ °C cm}^{-1}$ during the experiments.
 114 When partial melting of the sample was achieved, directional solidification was triggered, for sample B
 115 by pulling the sample down with a speed of 0.03 cm min⁻¹ ($5 \times 10^{-6} \text{ m s}^{-1}$), which corresponds to a cooling
 116 rate of 0.4 °C min⁻¹, and for sample A by applying a cooling rate of 0.4 °C min⁻¹ to both heaters for the
 117 first half of solidification followed by a cooling rate of 4 °C min⁻¹ for the second half of solidification. A
 118 total of five and four heating/cooling cycles were carried out for samples A and B, leading to exposure

119 times to temperatures above 1100 °C of 20 and 8 hours, respectively. In this study the last heating/cooling
120 cycle is discussed, as the grain structure is preserved for *ex situ* analysis. Although the growth processes
121 of sample A and B differ, we do not expect significant differences during crystal growth due to the three
122 following reasons. First, for both analyzed experiments in samples A and B, the measured growth rate
123 (measured directly thanks to the *in situ* imaging) is identical (within the measurement accuracy limits)
124 and the applied temperature gradient is also the same. Second, the diffraction images recorded during the
125 first experiments using cooling rate applied to both heaters in sample B show that the general
126 solidification features are reproducible compared to the last experiment using pulling down to initiate
127 solidification. Third, the grain structure observed in both samples A and B is comparable.
128

129 2.2. In situ observation

130 *In situ* and real-time observation of the melting and solidification processes was achieved by using X-
131 ray synchrotron radiation at beamline ID 19 of the European Synchrotron (ESRF) in Grenoble, France. A
132 combination of X-ray radiography and topography imaging allows studying the development of crystal
133 defects [29]. Two individual camera-based detector systems were used to monitor the radiographic and
134 topographic images with an image acquisition rate of 2 s⁻¹. The radiography image contrast results from
135 the density difference between the solid and the liquid phases and provides information on the dynamics
136 and the morphology of the solid-liquid interface. The topography image results from Bragg diffraction
137 and can be considered as one extended Laue spot that provides information on the crystal structure and
138 associated extended defects. Crystal imperfections such as deformations and dislocations change the
139 diffraction angle of the X-rays, resulting in superimpositions or gaps that are visible in the image as a
140 change in contrast. The observed contrast provides qualitative information on the strain level which is
141 associated with the macroscopic crystal deformation.

142 2.3. Ex situ analyses

143 After the *in situ* solidification experiments both surfaces of the samples were first polished with SiC
144 abrasive paper and then with a 6 μm and a 3 μm diamond suspension to remove the reaction layer of the
145 boron nitride crucible and to obtain a flat surface for EBSD analysis. EBSD was performed using a FEG-
146 SEM JEOL JSM 7001F operating at an acceleration voltage of 20 kV, a working distance of ~20.0 mm, a
147 tilt angle of 70° and several magnifications. The SEM was equipped with a HKL Nordlys camera driven
148 by the ‘Channel 5’ softwares suite (comprising ‘Flamenco’ for acquisition, ‘Map Stitcher’ for stitching,
149 ‘Tango’ for mapping and ‘Mambo’ for pole figures) using either a 7 μm or a 1 μm step size depending on
150 the studied area. Orientation maps parallel to the growth direction (x), perpendicular to the growth
151 direction (y) or normal to the sample surface (z) are displayed using the conventional inverse pole figure
152 (IPF) coloring. For both samples, the x direction corresponds to the growth direction. To obtain large-
153 scale maps, the individually scanned images were stitched together. In some cases, the individual images
154 do not fit together perfectly, which leads to visible stitching artefacts on the large-scale maps. Grain
155 boundaries with a special character are shown in coincidence site lattice (CSL) maps. Σ3 <111> GBs are
156 displayed in red, Σ9 <110> GBs in blue and Σ27a <110> GBs in yellow. Σ (Sigma) is the ratio between
157 the number of lattice points in the unit cell of the CSL lattice and the number of lattice points in the unit
158 cell of the generating lattice. The rotations around the indicated <hkl> directions satisfy the
159 misorientation ranges given by the Brandon criterion [30], which are (60 ± 8.66)°, (38.94 ± 5)° and (31.58
160 ± 2.89)° for Σ3, Σ9 and Σ27a GBs, respectively. The range within special grain boundaries are defined as
161 Σ grain boundaries is given by $\theta = 15^\circ/\sqrt{\Sigma}$. Additionally, misorientation maps that show small angular
162 deviations from a predefined crystallographic direction, are used to detect subgrains. The detection limit

163 of misorientation angles is approximately 0.5° for the EBSD analysis with the highest spatial resolution of
164 $1\ \mu\text{m}$ [31].

165 To reveal etch pits and grooves, the samples were etched for 5 min. with the chemical agent Sirtl
166 ($\text{HF}(40\%):\text{CrO}_3(5\text{M}) = 1:1$). The etching revealed grain boundaries and emerging dislocations that were
167 observed using an optical microscope. The etching was done twice: the first etching after the EBSD
168 measurements with $7\ \mu\text{m}$ resolution and the second etching after the EBSD measurements with $1\ \mu\text{m}$
169 resolution.

170 3. Results

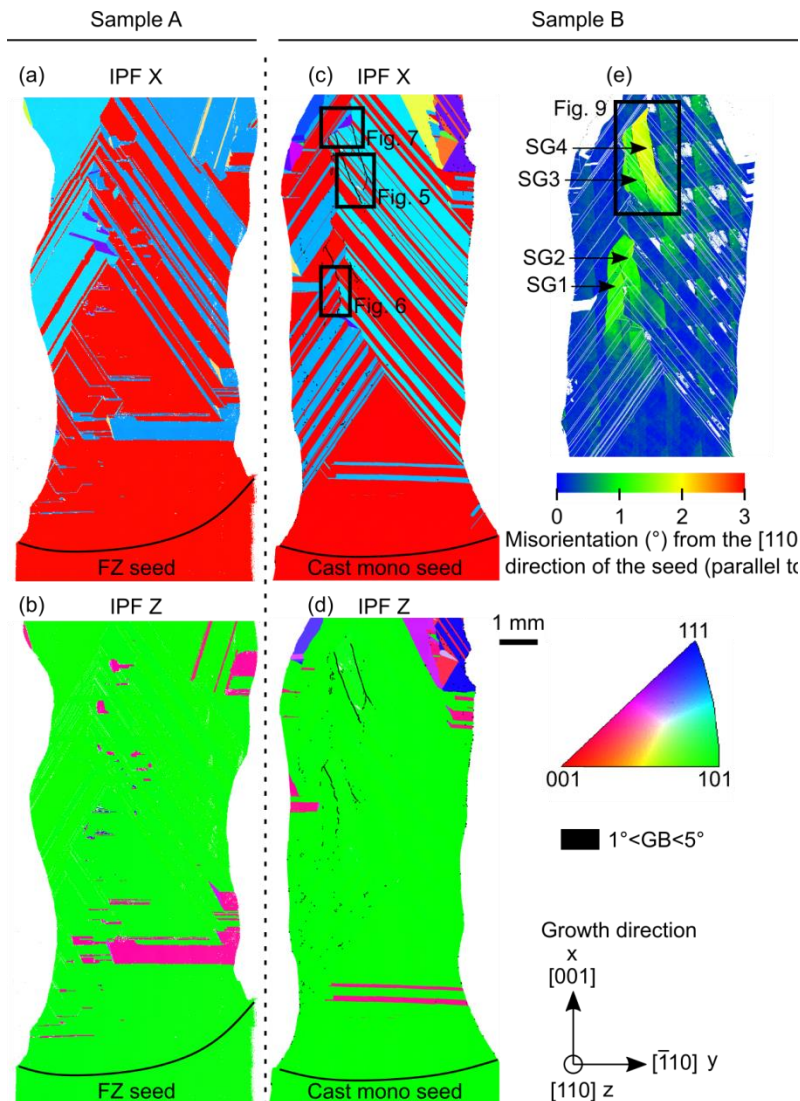
171 3.1. Grain structure

172 The overall grain structures of samples A and B are dominated by diagonal successive twinning from
173 both edges, represented in the IPF X images of Fig. 2(a) and (c), respectively. $\Sigma 3$ twinning at the edges
174 occurs because there exists a large undercooling [27] that facilitates the nucleation of twin grains [32].
175 The twin grains enter in competition at the center of the sample, though, the encounter is shifted towards
176 the left side in both samples. From the radiographs (see Fig. 3(a) for sample A), it can be deduced that the
177 twins nucleate earlier on the right side because the solid-liquid interface on the right side advances faster.
178 This behavior was also reported and explained for this kind of experiments in [33]. The competition
179 between the twins that propagate from both sides is accompanied by a significant amount of stress. This
180 becomes clear by looking at the topography images (Fig. 3(b) and Fig. 4(a) and (b) for samples A and B,
181 respectively), which show a very dark contrast area where the competition takes place. The dark contrast
182 (stress) started to build up at the level of the initial solid(seed)-liquid interface. Additional dark contrast is
183 observed on the left of Fig. 3(b), where several twinned grains nucleated as can be seen on the IPF X plot
184 of Fig. 3(c). However, the higher stress (enhanced black contrast) is observed at the position of encounter
185 and competition of the diagonal twins coming from the sides (Fig. 3(b)). It was also observed in our
186 previous work [33] in comparable solidification conditions in a different sample and during another
187 experimental campaign. In both samples the strain diminishes above in the crystal after the nucleation of a
188 new grain (purple in IPF X map of Fig. 2(a) and (c)), which is assumed to nucleates inside a grain
189 boundary groove created by the side twins in the sample center. It has a different crystallographic
190 orientation than the side twins and the seed grains. Its growth direction is close to $\langle 744 \rangle$. In Fig. 3 and
191 Fig. 4 these grains are encircled in black dotted lines. On top of them the global strain (dark contrast
192 areas) reduces, as was previously observed in experiments with a FZ-seed of the same crystallographic
193 orientation [33].

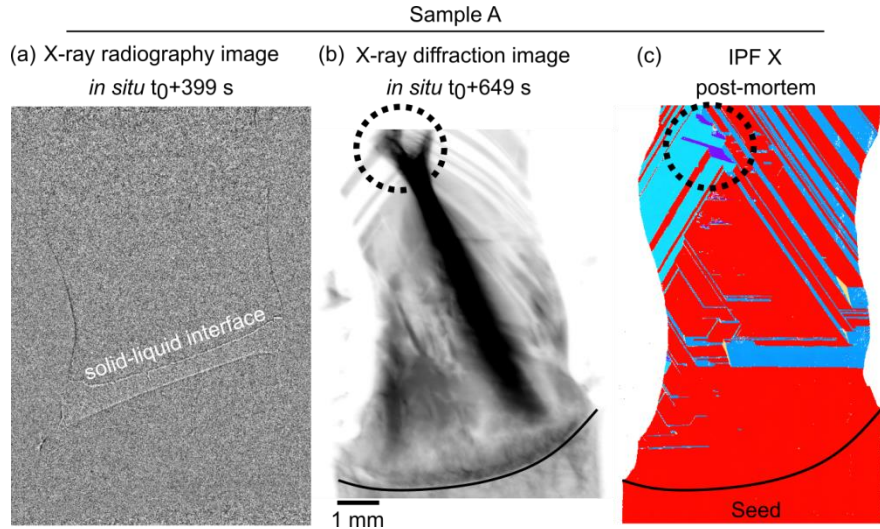
194 By looking at the IPF X and IPF Z images of both samples (Fig. 2(a)-(d)), it is apparent that the
195 overall grain structure is the same. The $[110]$ surface direction of the seed continues in the new grains
196 almost over the entire sample height. The main difference in the structure of both samples is the
197 development of high, up to 3° -misorientated subgrain domains in sample B, which are not present in
198 sample A. The subgrain domains are detectable on the EBSD orientation maps because they have slightly
199 different crystallographic orientations compared to the grain matrix. The black lines in Fig. 2(c) and (d)
200 and the green areas in Fig. 2(e) reveal the subgrains. Fig. 2(e) shows the degree of misorientation from the
201 $[110]$ direction of the seed crystal in different colors: dark blue means no misorientation with respect to
202 the reference direction and green, yellow and red mean a misorientation of 1° , 2° and 3° from the
203 reference seed direction, respectively. The reference direction corresponds to a direction that is nearly
204 parallel to the z-direction, i.e. normal to the sample surface.

205 Two subgrain domains (1 and 2) are evidenced. Considering the detection limit, the first subgrain
206 domain becomes visible ca. 5.8 mm above the seed-regrown silicon interface and consists of two
207 subgrains (SG1 and SG2). The second subgrain domain becomes visible ca. 12.5 mm above the seed-

208 regrown silicon interface and consists also of two subgrains (SG3 and SG4). The subgrains are finite and
 209 disappear again after a few millimeters.
 210



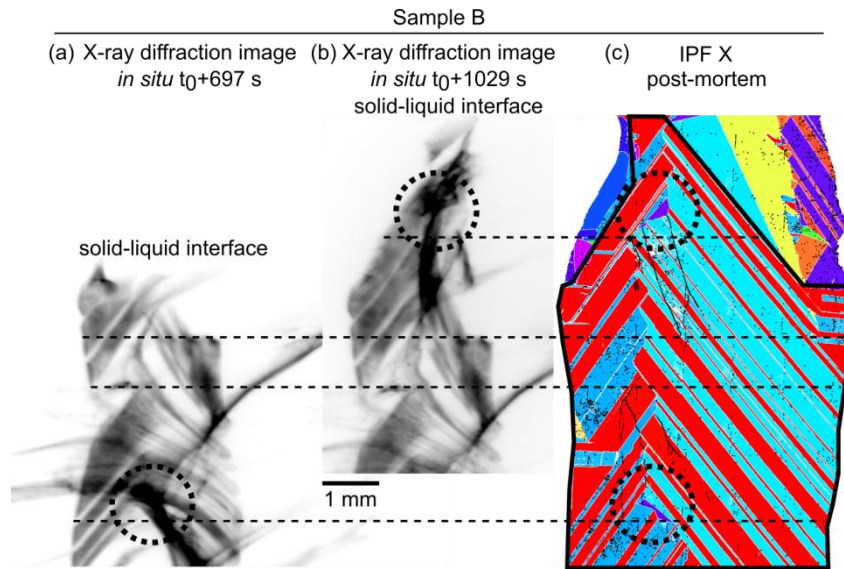
211
 212 **Fig. 2** (a) and (c) IPF X and (b) and (d) IPF Z orientation maps obtained by EBSD measurements of the solidified
 213 samples A (FZ-seeded) and B (cast mono-seeded), respectively. (e) The map shows the degree of misorientation
 214 from the [110] direction of the seed crystal. In sample B, SGBs are observed that show misorientations up to 2° with
 215 respect to the seed orientation (see also black-lines in (c) and (d)). The color gradations within the individual
 216 rectangles are due to map stitching artefacts and due to deviations of the electron beam during large-scale map
 217 acquisition.



218

219 **Fig. 3** (a) *In situ* X-ray radiography image, (b) *in situ* X-ray topography image and (c) post-mortem IPF X
 220 orientation map of the FZ-seeded sample A. The X-ray radiography image was post-processed to better visualize the
 221 solid-liquid interface. The dark circle indicates a new grain nucleation (purple grain in (c)), which correlates to the
 222 reduction of strain in (b). $t_0 = 0$ corresponds to the start of solidification.

223



224

225 **Fig. 4** (c) IPF X orientation map with (a) and (b) corresponding to *in situ* X-ray diffraction snapshots at different
 226 processing times of the cast mono-seeded sample B. $t_0 = 0$ corresponds to the start of solidification. The red [001]
 227 grains that lie in the black framed area of the orientation image are visible on the diffraction images. The circles
 228 indicate the locations of new grain nucleations (purple grains) that contribute to recovery of lower strain levels in the
 229 upper growing grains (reduction of the dark contrast area in the X-ray diffraction images). The dashed lines serve as
 230 guides to the eyes to recognize corresponding regions.

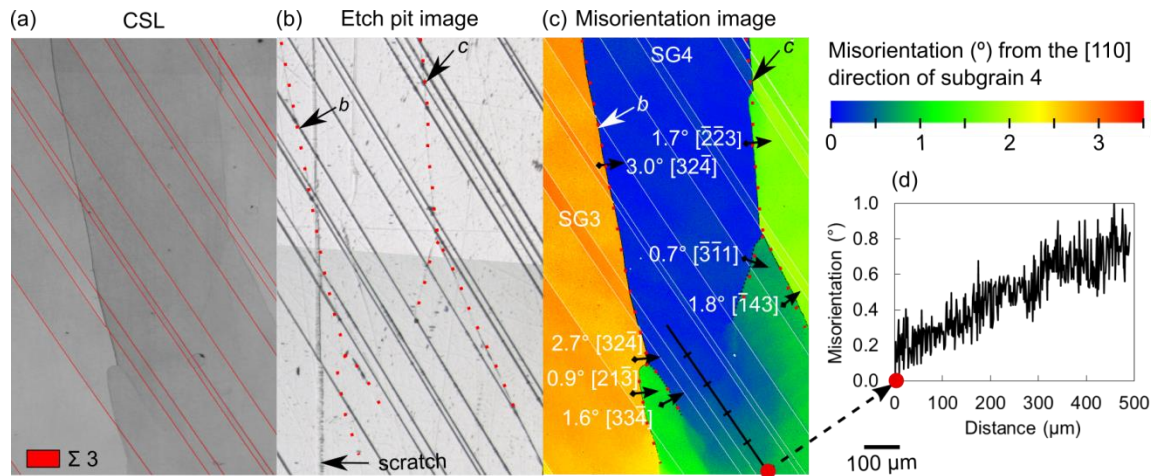
231 3.2. Formation of SGB domains

232 In Fig. 5 the formation area of subgrain 4 is shown. The CSL map (Fig. 5(a)) shows that the region
 233 consists of diagonally arranged $\Sigma 3$ twins. Figure 5(b) is an optical etch pit image on which the dark
 234 diagonal lines represent the same twin boundaries. The red dotted lines show the traces of the SGBs that

235 are only weakly visible or in some places are not visible at all on the microscopic image after etching
 236 (Fig. 5(b)).

237 On the misorientation image of Fig. 5(c), the subgrains are clearly distinguishable because they
 238 exhibit a misorientation up to 3°. The image shows the degree of misorientation from the [110]
 239 with respect to subgrain 4. It can be seen that there is a misorientation of 3° between subgrains 3 and 4.
 240 The misorientation between subgrain 4 and the grain matrix is 1.7°. Below the sample height at which
 241 the SGBs become visible, a continuous increase of the misorientation can be measured along with the
 242 growth direction (Fig. 5(c)). Furthermore, at the lower ends of the SGBs *b* and *c*, which delimit subgrain
 243 4, two SGB-branches initially merged into one SGB.

244 The misorientation angle of SGB *b* is the sum of the misorientation angles of the two initial branches.
 245 A summation occurred because the two branches separate subgrains that have a similar misorientation
 246 axis ($[21\bar{3}]$ compared to $[33\bar{4}]$). This supports the assumption that the two branches converged into one
 247 during solidification to form a SGB with a higher misorientation. This suggests that the dislocations
 248 incorporated in the SGB are of the same character. When the branches of SGB *c* merge, the
 249 misorientation is not the sum of both. The reason is that the misorientation axis of both branches differ
 250 ($[\bar{3}\bar{1}1]$ compared to $[\bar{1}43]$). In this case, the dislocations are probably of different character.
 251



252 **Fig. 5** (a) CSL map, (b) etch pit image and (c) misorientation map of the formation area of subgrains 3 and 4. The
 253 degree of misorientation from the [110] direction of subgrain 4 is shown. (d) The graph shows a continuous increase
 254 of misorientation along the black line.
 255

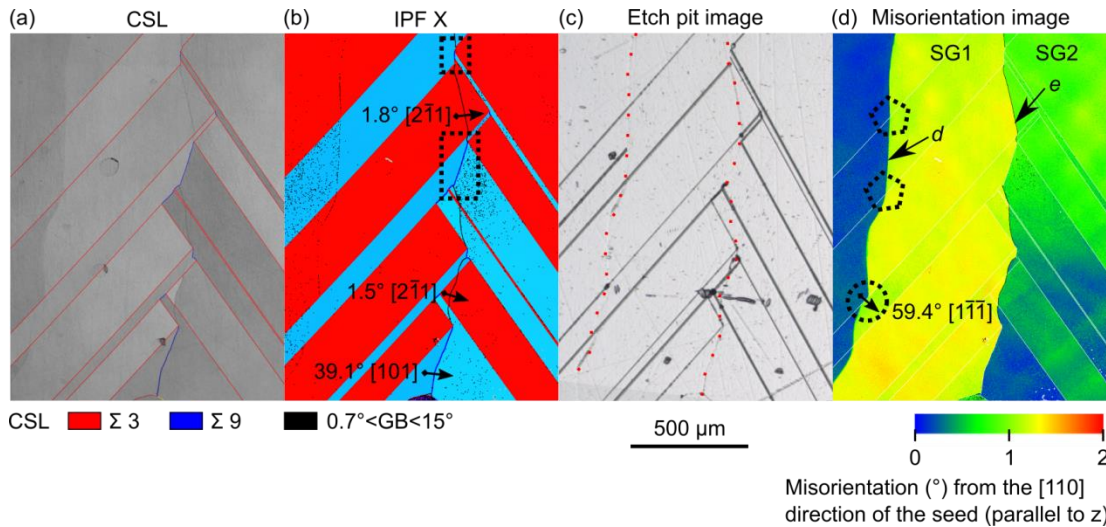
256 3.3. Propagation of SGBs

257 Once a SGB is formed, it evolves almost perpendicular to the solid-liquid interface. In Fig. 6 the
 258 propagation of SGBs *d* and *e*, which separate subgrains 1 and 2, are shown. Figure 6(a) is the CSL map
 259 and Fig. 6(b) an inverse pole figure map along the x-direction (corresponding to the growth direction).
 260 Figure 6(c) is an optical etch pit image, where the dotted red lines mark the trace of the SGBs observed
 261 with EBSD. As was shown before, the SGBs are faintly visible on the etch pit image. Figure 6(d) shows
 262 the degree of misorientation from the [110] direction with respect to the grain matrix.

263 SGB *d* follows the direction of growth and crosses $\Sigma 3\{111\}$ GBs without producing noticeable
 264 changes (see dotted pentagons in Fig. 6(c)). Along some short segments, SGBs also follow $\Sigma 3\{111\}$ GBs
 265 (see dotted circle in Fig. 6(c)). It causes the $\Sigma 3$ GB $\{111\}$ to become an incoherent GB, which is expressed
 266 by the misorientation angle that deviates from 60°.

267 SGB *e* is located in a region where grain competition among grains that grow from both sides takes
 268 place. Either $\Sigma 3$ or $\Sigma 9$ GBs are formed depending on the twin relationship. A difference in the interaction

269 behavior between the SGB and $\Sigma 3$ and $\Sigma 9$ GBs can be seen. We find that SGBs never cross $\Sigma 9$ GBs, but
 270 follow them (see dotted rectangles in Fig. 6(b)). We also observe that the misorientation angle of SGB *e*
 271 increases from 1.5° to 1.8° towards the top.
 272



273
 274 **Fig. 6** (a) CSL map, (b) IPF X orientation map, (c) etch pit image and (d) misorientation map showing the
 275 interaction of SGBs with $\Sigma 3$ and $\Sigma 9$ grain boundaries.

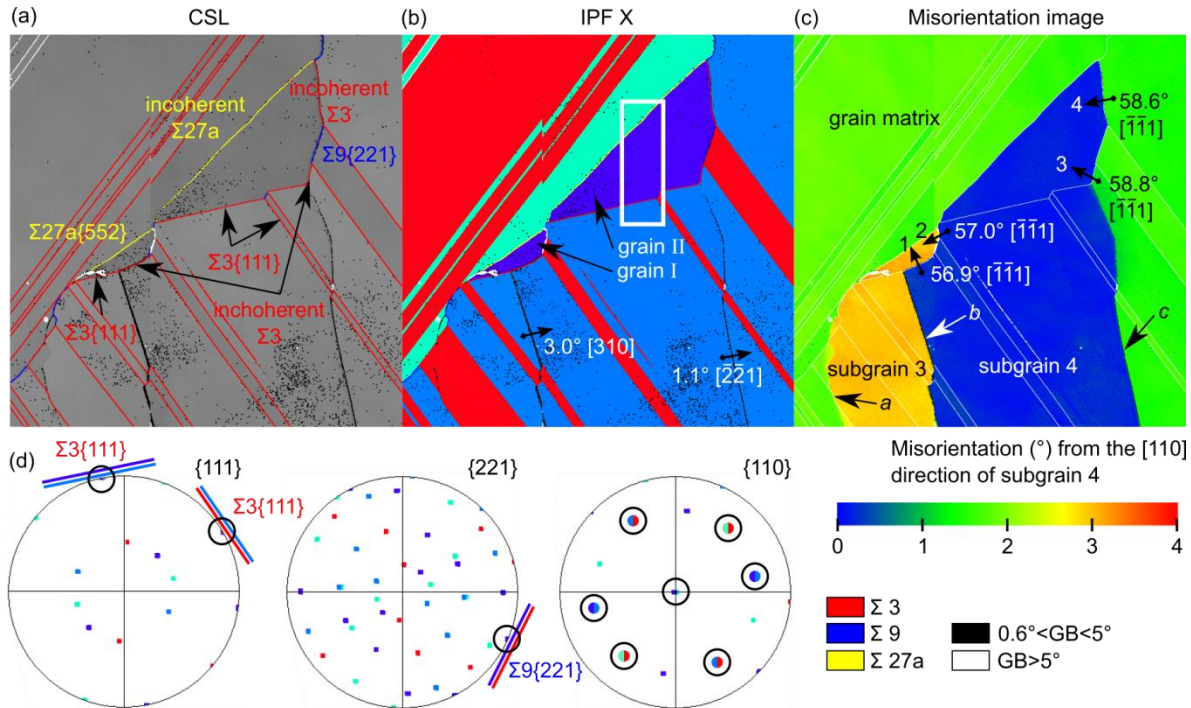
276 *3.4. Disappearance of SGBs*

277 The disappearance of both subgrains 3 and 4 is associated with the nucleation of new grains of the
 278 same $\langle 744 \rangle$ type (grains I and II in Fig. 7). Nucleation of grains I and II takes place on $\Sigma 3\{111\}$ facets
 279 included within the subgrains 3 and 4, respectively. This is why they have the same crystallographic
 280 misorientation with respect to the matrix than the entire subgrain area (see Fig. 7(c)). The nucleation
 281 events of grains I and II takes place in the subgrain areas 3 and 4 on the contrary to all other previous
 282 nucleation occurring during growth. Before these nucleation events, the subgrains grew only by an
 283 upward propagation crossing grains that nucleated far away from the subgrain area (at the sides of the
 284 sample). Although grain nucleation can be triggered by the presence of dislocations and/or deformed
 285 areas [27, 33] and by extension possibly by the presence of SGBs, it is not possible to conclude on this
 286 from our experiments. Moreover, it is worth noting that the same kind of nucleation events (same
 287 crystallographic orientation and position) was observed in sample A in which SGBs were absent.

288 In order to understand why the subgrains disappear, it is necessary to have a detailed look at the
 289 development of the three SGBs *a*, *b* and *c*, which delimit subgrains 3 and 4 laterally. SGB *a* stops at the
 290 encounter of grain I. SGBs *b* and *c* meet the new grains I and II at a $\Sigma 3\{111\}$ GB. In both cases, they do
 291 not cross the GB but propagate along the GB inducing a direction change.

292 The $\Sigma 3$ GB is modified from a coherent $\Sigma 3\{111\}$ to an incoherent $\Sigma 3\{111\}$ GB. This is reflected in
 293 the misorientation angles of 56.9° (arrow 1 in Fig. 7(c)) and 58.8° (arrow 3 in Fig. 7(c)) between grains I
 294 and II and their neighbor grains, respectively, to be compared to the value of 60° expected for a perfect
 295 $\Sigma 3$ GB. These grains have a $\langle 744 \rangle$ orientation close to the growth direction. The misorientation of the
 296 incoherent $\Sigma 3$ GB below grain I is higher than that on the right side of grain II. This is due to the fact that
 297 the misorientation of SGB *b* is higher, too. Following the grain boundaries to the upper right, the
 298 misorientation remains unchanged. Interrupted by $\Sigma 9$ GBs, the next incoherent $\Sigma 3$ GBs have similar
 299 misorientations of 57.0° (arrow 2 in Fig. 7(c)) and 58.6° (arrow 4 in Fig. 7(c)), respectively. This is
 300 consistent with the misorientations of the SGBs measured before (3.0° and 1.1° for *b* and *c*, respectively).

301 Then, the SGBs encounter a triple junction between an incoherent $\Sigma 3$, and a $\Sigma 27a$ GB. In fact, it is the
 302 first time during their upward propagation that the SGBs meet a $\Sigma 27a$ GB. After the encounter they do not
 303 continue their way in the direction of growth. The formation of the $\Sigma 27a$ GBs is associated with the
 304 nucleation of the new grains I and II that form a $\Sigma 27a$ GB on top. Since $\Sigma 27a$ GBs are also observed in
 305 sample A, which has no subgrains, these $\Sigma 27a$ GBs are only the result of grain competition.
 306



307
 308 **Fig. 7** (a) CSL map, (b) IPF X orientation map, (c) misorientation map and (d) $\{111\}$, $\{221\}$ and $\{110\}$ pole figures
 309 of the grains lying inside the white rectangle of map (b). The dark circles encircle common crystallographic
 310 directions.

311 3.5. Dislocations in the seed crystals

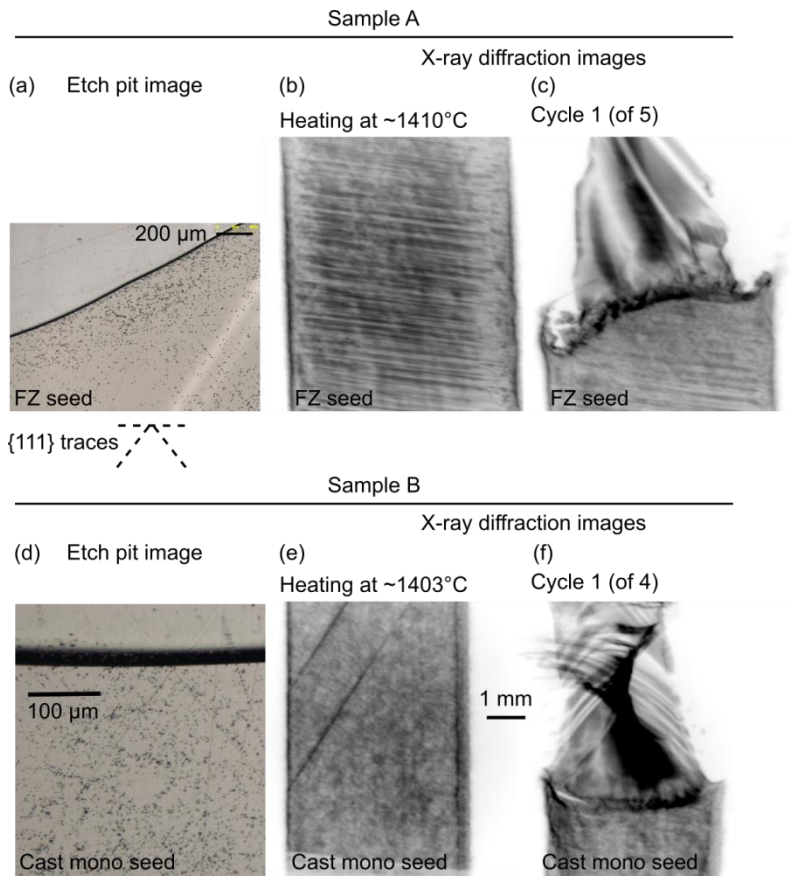
312 Dislocation distributions were observed by etching and by X-ray diffraction imaging. Dislocation
 313 densities measured by etch pit counts only show dislocations that emerge at the surface. Dislocations that
 314 stay in planes parallel to the sample surface are not revealed. In the diffraction images, dislocations are
 315 not visible if they fulfill the extinction criterion $\mathbf{b} \cdot \mathbf{g} = 0$ for the particular diffraction spot observed (\mathbf{b} is
 316 the Burgers vector and \mathbf{g} is the diffraction vector). Therefore, both techniques do not represent the total
 317 amount of dislocations, but give a qualitative indication of the amount.

318 Figures 8(a) and (d) show etch pit images of samples A and B at the position of the seed-regrown
 319 interface. In Fig. 8(b) and (e) *in situ* diffraction images of both samples are presented that show the seed
 320 crystals shortly before melting. The etch pits on the cast mono seed (sample B) form an array of
 321 dislocation cells. In the FZ seed the dislocation are not arranged in cells and are more widely spread. The
 322 dislocations are arranged in lines, which follow the traces of two crossing $\{111\}$ family planes that are
 323 oriented perpendicular to the surface. Finally, the dislocation density is higher in sample B-seed compared
 324 to sample A-seed.

325 The diffraction images confirm the observation from the etch pits images. The cast mono seed shows
 326 a dense network of dislocations arranged in cells compared to the FZ-seed. The time sequence of the *in*
 327 *situ* X-ray images reveal that the dislocations are not very mobile during heating and up to the melting

328 point in sample B compared to sample A (videos that show the heating phases of sample A and B are
 329 available as supplementary material). The two diagonal dark lines are probably micro-twins. In the FZ
 330 seed the dislocations originating from sources at the sample edges are very mobile up to the silicon
 331 melting point and move on different $\{111\}$ planes. The almost horizontal lines form because dislocations
 332 propagate on the $[111]/[\bar{1}\bar{1}\bar{1}]$ and $[\bar{1}\bar{1}\bar{1}]/[111]$ planes, whose projection traces at the surface plane are
 333 horizontal. As these planes have an angle of 35.3° with the surface $\{110\}$ planes, the movement of the
 334 dislocations on the planes can be nicely observed on the projected images. The propagation of
 335 dislocations along these planes is activated by the pressure exerted by the crucible on the main surface
 336 sides [34]. The reason for the slight inclination of the “horizontal” lines by 8° is due to a geometric
 337 distortion during recording, which is explained in [29]. Activation of the two $\{111\}$ planes that are
 338 perpendicular to the surface can only be seen close to the melting point. These are the diagonal lines
 339 ($\{111\}$ traces) that are also observed on the etch pit image.

340 What both samples have in common is that the etch pit density significantly reduces from the non-
 341 molten seed to the new grown crystal. In Fig. 8(c) and (f), topography images of samples A and B shortly
 342 after the first solidification cycle are shown. The seed-regrown interface is very dark and therefore
 343 distorted. Inside the new grown grains dark areas are present as well. Although individual dislocations are
 344 poorly visible, one can see that the dislocation structure is quite different in the new grown crystals:
 345 neither horizontal dislocation lines for sample A, nor dislocation cells for sample B are visible.
 346



347
 348 **Fig. 8** (a) and (d) post-mortem etch pit images of the initial solid-liquid interface of the last cooling cycle of samples
 349 A and B, respectively. (b) and (e) X-ray diffraction images of the unmolten seeds of samples A and B, respectively,
 350 shortly before melting. (c) and (f) X-ray diffraction images after the first cooling cycles of samples A and B,
 351 respectively, that show the seeds and the regrown crystals and their different dislocation arrangements.

352

353 4. Discussion

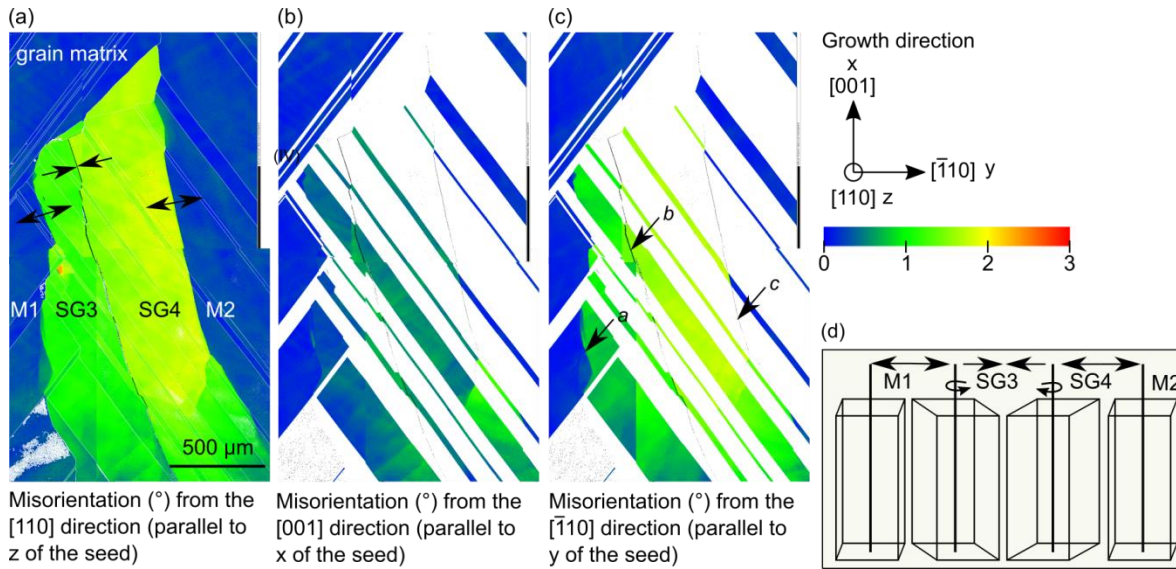
354 4.1. SBG structure

355 4.1.1. Orientation relationship of the subgrains

356 The SGBs in sample B are rotated towards each other mainly by a rotation around the [001] axis, i.e.
 357 the growth direction. This is illustrated in Fig. 9, where the degrees of misorientation from the [110], the
 358 [001] and the $[\bar{1}10]$ directions with respect to the seed orientation are shown from (a) to (c), respectively.
 359 In the x- and y-representations only the grains that have an orientation close to the original orientation of
 360 the seed can be seen in color because the other grains have a higher misorientation than 3° . The subgrains
 361 show a low misorientation along the x-direction but a similar high misorientation along the y- and z-
 362 directions consistent with tilt GBs. In Fig. 9(d) the inclination of the subgrains 3 and 4 relative to the
 363 grain matrix on both sides is schematically shown.

364 The fact that almost no etch pits are visible along the SGBs means that the dislocations do not emerge
 365 at the surface. Hence, it supports the point that the dislocation lines of the SGBs are mainly oriented along
 366 the growth direction. Since the rotation axis is principally along the growth direction, many dislocations
 367 have an edge character. This is consistent with the analysis of Lantreibecq et al. [18] who found that the
 368 SGBs in the source cast mono ingot are mainly composed of dislocations with a [001] line character and a
 369 Burgers vector $a/2[1\bar{1}0]$. They proposed that these dislocations grow by epitaxy on the solid-liquid
 370 interface. They also found two other families of dislocations that have Burgers vectors at 45° from the
 371 growth axis. These dislocations could be responsible for deviations of the tilt direction of the subgrains
 372 also observed in this study.

373



374

375 **Fig. 9** Misorientation maps show the degree of misorientation from the (a) [110], (b) [001] and (c) $[\bar{1}10]$ direction
 376 with respect to the seed orientation. (d) Schematic representaiton of the tilt directions of the two subgrains
 377 SG3 and SG4 and the matrix grains on the left and right side. SGB3 and SG4 are inclined towards each other.

378

379

4.1.2. SGB misorientations and their dislocation density

380 For SGB *b* we observe a continuous increase of the misorientation angle in the direction of growth,
 381 which is consistent with an accumulation of dislocations in a dislocation wall. This is also supported by
 382 our observation that lower misoriented branches merge to form a higher misoriented SGB in the direction
 383 of growth (cf. Fig. 5). A similar branched structure was earlier reported by Chuang et al. who observed
 384 SGB formation in silicon *in situ* suggesting that dislocations aggregate at the solid-liquid interface and
 385 increase the misorientation angle through the continual incorporation of new dislocations [2]. The
 386 branched dislocation arrays that merge into one SGB, the increase of the SGB misorientation and their
 387 principle orientation and tilt along the growth axis suggest a SGB formation during growth. SGBs aligned
 388 along the growth direction in mc-ingots have also been reported by other authors, who also assumed a
 389 generation of dislocations during growth at the solid-liquid interface [8, 13].

390 The distance between individual dislocations *d* assuming that the SGB is constituted of perfect edge
 391 dislocations aligned along the SGB can be evaluated by

392

$$d = \mathbf{b}/\sin(\theta).$$

393 Using $\mathbf{b} = 0.384$ nm for the Burgers' vector magnitude in silicon along a $\langle 110 \rangle$ direction, the distance
 394 between each dislocation is $d_1 = 7.3$ nm and $d_2 = 22$ nm for θ of 3° and 1° , respectively. These
 395 misorientation angles are in the same order of magnitude as what was observed by Lantreibecq et al. in
 396 the source cast mono ingot at a height of about 160 mm from the melt-back surface [18], which is above
 397 the area where electrically active subgrains do appear on the PL maps (cf. Fig. 1). The rotation axis is also
 398 similar.

399 The spacing of the dislocations can be used to estimate the number of dislocations within the SGBs.
 400 With a sample thickness $t = 3 \times 10^{-2}$ cm and a dislocation spacing in the order of $d_1 = 1 \times 10^{-6}$ cm, 3×10^4
 401 dislocations exist within SGB *b* assuming a Burgers vector of 0.384 nm standard for hypothetical edge
 402 dislocations aligned vertically constituting the boundary. Accordingly, approximately 1.5×10^4
 403 dislocations exist in SGB *a* and *c*, respectively. This makes a total of 6×10^4 dislocations that should
 404 intersect a horizontal virtual surface to create the observed boundary misorientations.

405

4.2. SGB origin and implications of the crystal quality of the seeds

406 Oriwol et al. [12] performed a detailed study on the origin of dislocation clusters and found that 97%
 407 originate at grain boundaries. Different from this report and from other studies [e.g. 9, 35], SGBs start in
 408 the bulk crystal and not at a specific GB in our experiment. One reason for the high number of
 409 dislocations in sample B could be that dislocations propagate from the seed in the regrown crystal.
 410 Dislocation density was measured in the range 1×10^4 cm⁻² to 3×10^4 cm⁻² in another brick of the source
 411 ingot at a similar height to the one at which the sample was extracted for our experiments. Such a
 412 dislocation density results in a maximum of 540 dislocations crossing each sample horizontal surface.
 413 Compared to a number of 6×10^4 dislocations for the regrown part of sample B, the density in the seed
 414 crystal is too low to be the origin of all dislocations associated with the subgrains. Another argument
 415 against the idea that all dislocations originate from the seed is that the etch pit structure changes above the
 416 seed-regrown interface, which indicates that there is either a reduction of the total number of dislocations
 417 or a change in dislocation character and orientation or both. Hence, there are not enough dislocations in
 418 the seed to create the observed misorientations and dislocation multiplication and not only accumulation
 419 must have taken place in the regrown part.

420 The question arises about the reason for the dislocation generation in sample B and not in sample A.
 421 That FZ-seeded samples do not develop subgrains has been confirmed several times by similar
 422 experiments using FZ seeds [33, 36]. When considering the two seeds A and B, it is obvious that a main

423 difference lies in the initial dislocation density and structuration. The initial dislocation network in the
424 cast mono seed at the melting point shows a low mobility and is arranged in a cellular structure, whereas
425 the dislocation network in the FZ seed is very mobile and aligned on $\{111\}$ glide planes.

426 In comparison to the source cast mono ingot of sample B, very similar subgrains are observed
427 indicating a similar origin. Since sample B was taken from a domain just below SGB multiplication
428 started in the source ingot, we can conclude that subgrain formation occurs at a similar height in both
429 cases. As only the cellular dislocation structure and microtwins are initially characterized in sample B
430 (see Fig. 8(e)), one of those defects might carry some deformation in relation with the SGB generation.
431 Additionally, as microtwins are not present anymore after our melting step, we hypothesize that the origin
432 of the SGB development could be due to the cellular dislocation structure present in the seed.

433 Besides the dislocation structure, another difference is the chemistry of the cast mono compared to the
434 FZ seed. The oxygen concentration in both seeds is very low, but the cast mono seed contains more
435 carbon than the FZ seed. However, the sample is not oversaturated in carbon so that only a small number
436 of precipitates should be present. It was reported that precipitates in the source cast mono seed do not
437 immobilize dislocations, but that they can create dislocation cross-slip, if they are exposed to sufficient
438 stress [18]. A strong influence of C- and N-based impurities on subgrain formation is therefore not
439 suspected. In addition, both samples have boron concentrations $>10^{17}$ at. cm⁻³ due to contact with the
440 boron nitride crucible. Since both samples are equally exposed to the boron nitride crucible, a different
441 influence behavior of boron on the formation of subgrains is improbable.

442 The clearly different dislocation structures of the two seeds A and B indicates that it is probably the
443 decisive factor causing the formation of subgrains. Unfortunately, it is not possible to give more
444 information on the origin of the subgrains, because subgrains with smaller misorientations that probably
445 exist in the lower part of the sample as it was reported in [18] could not be detected during this study due
446 to experimental limitations. In a next step, the recording multiple diffraction spots providing
447 complementary information is foreseen to clarify further details about the generation of subgrains.

448 4.3. SGB propagation and termination

449 The grain orientation relationship and the GB character play an important role for the propagation of
450 the SGBs. Once the SGBs are generated, they cannot leave the sample because they grow with the solid-
451 liquid interface and are arranged parallel to the growth direction. When meeting a grain boundary, the
452 existence of a common slip system on both sides of the grain boundary is necessary for dislocations to
453 cross the twin boundary. $\Sigma 3\{111\}$ GBs that separate $\{110\}\langle 001\rangle$ (red) and $\{110\}\langle 221\rangle$ (blue) oriented
454 grains are crossed by the SGBs without inducing any visible changes (colors refer to the IPFs). $\Sigma 3\{111\}$
455 GBs that separate $\{110\}\langle 221\rangle$ (blue) and $\{110\}\langle 744\rangle$ (purple) oriented grains are not crossed, but
456 change the direction of the SGBs. SGBs propagate rather along the $\Sigma 3$ and $\Sigma 9$ GBs limiting the purple
457 grains than through the purple grains. This is plausible as dislocations can be absorbed in a GB, splitting
458 into grain boundary dislocations (GBD) with smaller Burgers vectors, and move in the boundary [37, 38].
459 We observe that $\Sigma 3\{111\}$ GBs become incoherent GBs when SGBs merge with them and follow them.
460 This observation is different from the *in situ* observations of Chuang et al., who detected only cases where
461 SGBs crossed $\Sigma 3\{111\}$ GBs that remain coherent according to EBSD detection limits [39].

462 Notably, the orientation relationship of the blue and purple grains is not favorable for the dislocations
463 in the SGB to cross. It was reported by Schmid et al. that a common slip system is not enough to explain
464 the correlation between dislocations and grain boundaries, but that the structure of the grain boundaries
465 has to be taken into account [40]. From a macroscopic point of view, there is no difference in the
466 character of the crossed and uncrossed GBs. From a microscopic point of view, the GB structure is
467 unknown and TEM measurements would be required to obtain this information. In addition, it depends on
468 the local stress and on the type of dislocation whether it can pass through a grain boundary [41, 42]. It has

469 been observed [41] and simulated [43] that even $\Sigma 3\{111\}$ GBs can act as accumulation obstacles for
470 dislocations. The stereographic projection in Fig. 7(d) shows that the common $\langle 110 \rangle$ direction of the
471 red/blue grains is roughly oriented in the direction of the SGB path. The common $\langle 110 \rangle$ direction of the
472 blue/purple grains, however, is almost perpendicular to the SGB direction, i.e. parallel to the solid-liquid
473 interface. The highest probability of crossing for dislocations and thus for dislocations arranged in a SGB
474 is obtained if there is a common glide plane (common $\langle 110 \rangle$ direction) if other conditions of stress and
475 dislocation character are fulfilled. Consequently, as the growth direction is forced upon the grains by the
476 temperature gradient, the unsuitable orientation of the common $\langle 110 \rangle$ direction might be the reason for
477 the SGB change, especially if there is no Burgers vector common to both slip systems.

478 Above the purple grains, the SGBs do not continue their way. Either dislocations rearrange at the
479 level of high disorder twin boundaries, like $\Sigma 27a$ GBs that limit the purple grains on top and emit new
480 dislocations, or the dislocations leave the sample by cross slipping at the $\Sigma 3$ or $\Sigma 9$ GBs. $\Sigma 27a$ GBs have a
481 higher boundary energy than $\Sigma 3$ and $\Sigma 9$ GBs and were found to be the source of new dislocations [13, 14,
482 35] probably as the result of atomic faceting [44, 45]. We do not observe any new dislocation emissions
483 originating at these $\Sigma 27a$ GBs, but first, the *in situ* X-ray diffraction image is very dark at this position,
484 which conceals the observation of dislocations, and second, new generated dislocations could grow out of
485 the sample surface due to the thin sample geometry.

486 It is also important to note that these purple grains were identified as the grains whose nucleation
487 releases strain previously accumulated as a result of grain competition when no SGBs are observed [33].
488 The new grain nucleation leads to a subsequent grain structure reorganization, which contributes to a
489 reduction of the strain in the growing ingot. Although the disappearance of the subgrain domain is
490 probably affected by the thin sample geometry, it means that the purple grains have an unambiguous
491 influence on the SGB evolution. In a large-scale casting it could be a mechanism to stop or spread SGBs.
492

493 5. Conclusion

494 *In situ* growth experiments and *ex situ* analyses of two seeded wafers were performed. The initial seed
495 orientation along the growth direction was [001] for both the FZ and the cast mono seeds. Several
496 millimeters long subgrain boundaries, elongated in the growth direction and crossing a number of twin
497 boundaries are formed in the cast mono-seeded sample, but not in the FZ-seeded sample. The subgrains
498 have a main rotation axis along the [001] growth direction and increase their misorientation by merging
499 with new SGBs appearing in their vicinity.

500 *In situ* X-ray topography imaging during the heating and solidification experiments showed that the
501 dislocations are very mobile in the FZ seed and propagate on $\{111\}$ slip planes, whereas the dislocations
502 in the cast mono seed are less mobile and are arranged in cells. The significantly smaller number of
503 dislocations in the cast mono seed compared to the number of dislocations contained in the SGBs shows
504 that dislocation multiplication mechanisms must have taken place in the regrown part. Although the
505 source of the dislocations could not be revealed, the observations suggest that subgrain formation is
506 related to the initial cellular dislocation structure in the cast mono seed.

507 Once formed, the SGBs either follow $\Sigma 9\{221\}$ and $\Sigma 3\{111\}$ GBs or cross $\Sigma 3\{111\}$ GBs. In the
508 situation where SGBs follow twin boundaries, the coherency of the $\Sigma 3\{111\}$ GBs is degraded due to the
509 presence of the SGBs. A particular situation is observed where a $\Sigma 3\{111\}$ GB that separates $\langle 221 \rangle$ and
510 $\langle 744 \rangle$ oriented grains constitutes an obstacle and is not crossed by the SGBs. Whether the dislocations
511 stop or cross-slip cannot be determined, because the sample is very thin and a change in direction of the
512 dislocation lines would cause the dislocations to escape at the surface. However, in either of these cases
513 the vertical SGB propagation in the growth direction is disturbed. Transferring this finding to a real size

514 casting, the nucleation of <744> oriented grains that are known to release strain could be responsible for
515 the stopping or lateral spreading of SGBs.

516

517 **Credit author statement**

518 **Maïke Becker:** Conceptualization, Investigation, Writing - Original Draft, Visualization, Funding
519 acquisition **Etienne Pihan:** Conceptualization, Investigation, Writing - Review & Editing **Fabrice**
520 **Guillon:** Methodology, Investigation, Resources, Data Curation, Writing - Review & Editing
521 **Laurent Barrallier:** Methodology, Resources, Writing - Review & Editing **Gabrielle Regula:**
522 Conceptualization, Methodology, Investigation, Writing - Review & Editing **Hadjer Ouaddah:**
523 Investigation **Guillaume Reinhart:** Investigation, Methodology **Nathalie Manginck-Noël:**
524 Conceptualization, Methodology, Investigation, Data Curation, Writing - Review & Editing, Supervision,
525 Project administration, Funding acquisition

526

527 **Acknowledgements**

528 The following funding is acknowledged: Agence Nationale de la Recherche (grant No. 14-CE05-
529 0046-01, CrySaLID project); Deutsche Forschungsgemeinschaft (scholarship No. BE 6627/ 1-1 to Maïke
530 Becker).

531

532 **References**

- 533 [1] K.E. Ekstrøm, G. Stokkan, R. Søndena, H. Dalaker, T. Lehmann, L. Arnberg, M. Di Sabatino,
534 Structure and dislocation development in mono-like silicon, *physica status solidi (a)*, 212 (2015) 2278-
535 2288.
- 536 [2] L.-C. Chuang, K. Maeda, H. Morito, K. Shiga, K. Fujiwara, Origin of small-angle grain boundaries
537 during directional solidification in multicrystalline silicon, *Materialia*, 3 (2018) 347-352.
- 538 [3] D. Hu, T. Zhang, L. He, H. Chen, D. Zhong, S. Cao, J. Gao, Y. Wan, The characteristics of sub-grains
539 in the mono-like silicon crystals grown with directional solidification method, in: 38th IEEE Photovoltaic
540 Specialists Conference, Austin, TX, 2012, pp. 002735-002738.
- 541 [4] V.A. Oliveira, H.C. Sio, A. Faujour, L. Piot, A. Chabli, D. Camel, Recombination Activity of 2D
542 Extended Defects in Monolike Silicon, *Energy Procedia*, 92 (2016) 755-763.
- 543 [5] Y. Zhang, Z. Li, Q. Meng, Z. Hu, L. Liu, Distribution and propagation of dislocation defects in quasi-
544 single crystalline silicon ingots cast by the directional solidification method, *Solar Energy Materials and*
545 *Solar Cells*, 132 (2015) 1-5.
- 546 [6] S. Zhou, C. Zhou, W. Wang, Y. Tang, J. Chen, B. Yan, Y. Zhao, Effect of Subgrains on the
547 Performance of Mono-Like Crystalline Silicon Solar Cells, *International Journal of Photoenergy*, 2013
548 (2013) 1-8.
- 549 [7] G. Stokkan, Y. Hu, Ø. Mjøs, M. Juel, Study of evolution of dislocation clusters in high performance
550 multicrystalline silicon, *Solar Energy Materials and Solar Cells*, 130 (2014) 679-685.
- 551 [8] D. Oriwol, M. Trempa, L. Sylla, H.S. Leipner, Investigation of dislocation cluster evolution during
552 directional solidification of multicrystalline silicon, *Journal of Crystal Growth*, 463 (2017) 1-9.
- 553 [9] D. Kohler, A. Zuschlag, G. Hahn, On the origin and formation of large defect clusters in
554 multicrystalline silicon solar cells, *Solar Energy Materials and Solar Cells*, 120 (2014) 275-281.
- 555 [10] S. Würzner, R. Helbig, C. Funke, H.J. Möller, The relationship between microstructure and
556 dislocation density distribution in multicrystalline silicon, *Journal of Applied Physics*, 108 (2010).
- 557 [11] F. Zhang, X. Yu, D. Hu, S. Yuan, L. He, R. Hu, D. Yang, Controlling dislocation gliding and
558 propagation in quasi-single crystalline silicon by using <110>-oriented seeds, *Solar Energy Materials and*
559 *Solar Cells*, 193 (2019) 214-218.
- 560 [12] D. Oriwol, M. Hollatz, M. Reinecke, Control of Dislocation Cluster Formation and Development in
561 Silicon Block Casting, *Energy Procedia*, 27 (2012) 66-69.

562 [13] B. Rynningen, G. Stokkan, M. Kivambe, T. Ervik, O. Lohne, Growth of dislocation clusters during
563 directional solidification of multicrystalline silicon ingots, *Acta Materialia*, 59 (2011) 7703-7710.

564 [14] T. Ervik, M. Kivambe, G. Stokkan, B. Rynningen, O. Lohne, Dislocation formation at E27a
565 boundaries in multicrystalline silicon for solar cells, in: 26th European Photovoltaic Solar Energy
566 Conference and Exhibition, 2011, pp. 1895-1899.

567 [15] M. Kivambe, G. Stokkan, T. Ervik, B. Rynningen, O. Lohne, TEM Characterization of near Sub-
568 Grain Boundary Dislocations in Directionally Solidified Multicrystalline Silicon, *Solid State Phenomena*,
569 178-179 (2011) 307-312.

570 [16] M.G. Tsoutsouva, V.A. Oliveira, D. Camel, J. Baruchel, B. Marie, T.A. Lafford, Mono-like silicon
571 ingots grown on low angle misoriented seeds: Defect characterization by synchrotron X-ray diffraction
572 imaging, *Acta Materialia*, 88 (2015) 112-120.

573 [17] T. Ervik, G. Stokkan, T. Buonassisi, Ø. Mjøs, O. Lohne, Dislocation formation in seeds for quasi-
574 monocrystalline silicon for solar cells, *Acta Materialia*, 67 (2014) 199-206.

575 [18] A. Lantreibecq, J.P. Monchoux, E. Pihan, B. Marie, M. Legros, Subgrains, micro-twins and
576 dislocations characterization in monolike Si using TEM and in-situ TEM, *Materials Today: Proceedings*,
577 5 (2018) 14732-14747.

578 [19] A. Krause, L. Sylla, D. Oriwol, Plastic deformation as an origin of dislocations in cast mono, *Enrgy*
579 *Proced*, 92 (2016) 833-838.

580 [20] M. Trempa, M. Beier, C. Reimann, K. Roßhirth, J. Friedrich, C. Löbel, L. Sylla, T. Richter,
581 Dislocation formation in seed crystals induced by feedstock indentation during growth of quasimono
582 crystalline silicon ingots, *Journal of Crystal Growth*, 454 (2016) 6-14.

583 [21] A. Lantreibecq, M. Legros, N. Plassat, J.P. Monchoux, E. Pihan, Spatial distribution of structural
584 defects in Cz-seeded directionally solidified silicon ingots: An etch pit study, *Journal of Crystal Growth*,
585 483 (2018) 183-189.

586 [22] V.A. Oliveira, M. Rocha, A. Lantreibecq, M.G. Tsoutsouva, T.N. Tran-Thi, J. Baruchel, D. Camel,
587 Cellular dislocations patterns in monolike silicon: Influence of stress, time under stress and impurity
588 doping, *Journal of Crystal Growth*, 489 (2018) 42-50.

589 [23] E. Nes, Recovery Revisited, *Acta Metall Mater*, 43 (1995) 2189-2207.

590 [24] G. Van Drunen, S. Saimoto, Deformation and recovery of [001] oriented copper crystals, *Acta*
591 *Metallurgica*, 19 (1971) 213-221.

592 [25] A. Tandjaoui, N. Mangelinck-Noel, G. Reinhart, B. Billia, X. Guichard, Twinning occurrence and
593 grain competition in multi-crystalline silicon during solidification, *Comptes Rendus Physique*, 14 (2013)
594 141-148.

595 [26] T. Riberi-Béridot, N. Mangelinck-Noël, A. Tandjaoui, G. Reinhart, B. Billia, T. Lafford, J. Baruchel,
596 L. Barrallier, On the impact of twinning on the formation of the grain structure of multi-crystalline silicon
597 for photovoltaic applications during directional solidification, *Journal of Crystal Growth*, 418 (2015) 38-
598 44.

599 [27] V. Stamelou, M.G. Tsoutsouva, T. Riberi-Béridot, G. Reinhart, G. Regula, J. Baruchel, N.
600 Mangelinck-Noël, {1 1 1} facet growth laws and grain competition during silicon crystallization, *Journal*
601 *of Crystal Growth*, 479 (2017) 1-8.

602 [28] T. Riberi-Béridot, M.G. Tsoutsouva, G. Regula, G. Reinhart, I. Périchaud, J. Baruchel, N.
603 Mangelinck-Noël, Growth undercooling in multi-crystalline pure silicon and in silicon containing light
604 impurities (C and O), *Journal of Crystal Growth*, 466 (2017) 64-70.

605 [29] M. Becker, G. Regula, G. Reinhart, E. Boller, J.-P. Valade, A. Rack, P. Tafforeau, N. Mangelinck-
606 Noël, Simultaneous X-ray radiography and diffraction topography imaging applied to silicon for defect
607 analysis during melting and crystallization, *Journal of Applied Crystallography*, 52 (2019) 1312-1320.

608 [30] D.G. Brandon, The structure of high-angle grain boundaries, *Acta Metallurgica*, 14 (1966) 1479-
609 1484.

610 [31] F.J. Humphreys, Review - Grain and subgrain characterisation by electron backscatter diffraction, *J*
611 *Mater Sci*, 36 (2001) 3833-3854.

612 [32] M.G. Tsoutsouva, T. Riberi – Béridot, G. Regula, G. Reinhart, J. Baruchel, F. Guittonneau, L.
613 Barrallier, N. Mangelinck-Noël, In situ investigation of the structural defect generation and evolution
614 during the directional solidification of $\langle 110 \rangle$ seeded growth Si, *Acta Materialia*, 115 (2016) 210-223.
615 [33] T. Riberi – Béridot, M.G. Tsoutsouva, G. Regula, G. Reinhart, F. Guittonneau, L. Barrallier, N.
616 Mangelinck-Noël, Strain building and correlation with grain nucleation during silicon growth, *Acta*
617 *Materialia*, 177 (2019) 141-150.
618 [34] M.G. Tsoutsouva, T. Riberi-Béridot, G. Regula, G. Reinhart, J. Baruchel, N. Mangelinck-Noël, In
619 Situ Imaging of Dislocation Expansion in FZ-Si Seeds During Temperature Ramp Heating Process,
620 *physica status solidi (a)*, 215 (2018).
621 [35] G. Stokkan, A. Song, B. Rynningen, Investigation of the Grain Boundary Character and Dislocation
622 Density of Different Types of High Performance Multicrystalline Silicon, *Crystals*, 8 (2018).
623 [36] H. Ouaddah, I. Périchaud, D. Barakel, O. Palais, M. Di Sabatino, G. Reinhart, G. Regula, N.
624 Mangelinck-Noël, Role of Impurities in Silicon Solidification and Electrical Properties Studied by
625 Complementary In Situ and Ex Situ Methods, *physica status solidi (a)*, 216 (2019).
626 [37] F. van An, N.A. Bulenkov, A.V. Andreeva, Structure of a second-order twin boundary in silicon and
627 its interaction with thermally generated lattice dislocations, *physica status solidi (a)*, 88 (1985) 429-441.
628 [38] L. Priester, J. Thibault, V. Pontikis, Theoretical, Numerical and Experimental Approaches for
629 Structural Studies of Grain Boundaries: Methods, Remarkable Results and Perspectives, *Solid State*
630 *Phenomena*, 59-60 (1998) 1-50.
631 [39] L.-C. Chuang, K. Maeda, H. Morito, K. Shiga, W. Miller, K. Fujiwara, Effect of misorientation angle
632 of grain boundary on the interaction with $\Sigma 3$ boundary at crystal/melt interface of multicrystalline silicon,
633 *Materialia*, 7 (2019).
634 [40] E. Schmid, S. Würzner, C. Funke, T. Behm, R. Helbig, O. Pätzold, H. Berek, M. Stelter, The
635 correlation between spatial alignment of dislocations, grain orientation, and grain boundaries in
636 multicrystalline silicon, *Crystal Research and Technology*, 47 (2012) 229-236.
637 [41] I. Yonenaga, K. Kutsukake, Transmission behavior of dislocations against $\Sigma 3$ twin boundaries in Si,
638 *Journal of Applied Physics*, 127 (2020).
639 [42] X. Baillin, J. Pelissier, J.J. Bacmann, A. Jacques, A. George, Dislocation transmission through $\Sigma = 9$
640 symmetrical tilt boundaries in silicon and germanium, *Philosophical Magazine A*, 55 (1987) 143-164.
641 [43] X. Chen, L. Xiong, A. Chernatynskiy, Y. Chen, A molecular dynamics study of tilt grain boundary
642 resistance to slip and heat transfer in nanocrystalline silicon, *Journal of Applied Physics*, 116 (2014).
643 [44] A. Autruffe, V. Stenhjem Hagen, L. Arnberg, M. Di Sabatino, Dislocation generation at near-
644 coincidence site lattice grain boundaries during silicon directional solidification, *Journal of Crystal*
645 *Growth*, 411 (2015) 12-18.
646 [45] A. Garg, W.A.T. Clark, J.P. Hirth, Dissociated and faceted large-angle coincident-site-lattice
647 boundaries in silicon, *Philosophical Magazine A*, 59 (1989) 479-499.
648